Supplementary Information

Molybdenum-enriched $Mo_{0.5}Ru_{0.5}O_2$ nanoparticles for efficient and stable oxygen evolution reaction

Kaizhu Zeng[1†], In Gyeom Kim[2†], Fangyuan Liu[1†], Peiyuan Gao[3], Litao Yan[2*], Bhuvana Modachur Sivakumar[2], Thomas W Wietsma[2], Yiheng Du[1], Qian Zhang[1], Chong Yang[1], Yang Hu[4], Tangyuan Li[1], Shu Hu[4,5,6], Yuyan Shao[2], Liangbing Hu[1,6,7*]

The supplementary information includes:

- Supplementary Figures 1−24
- Supplementary Tables 1−4
- Supplementary References

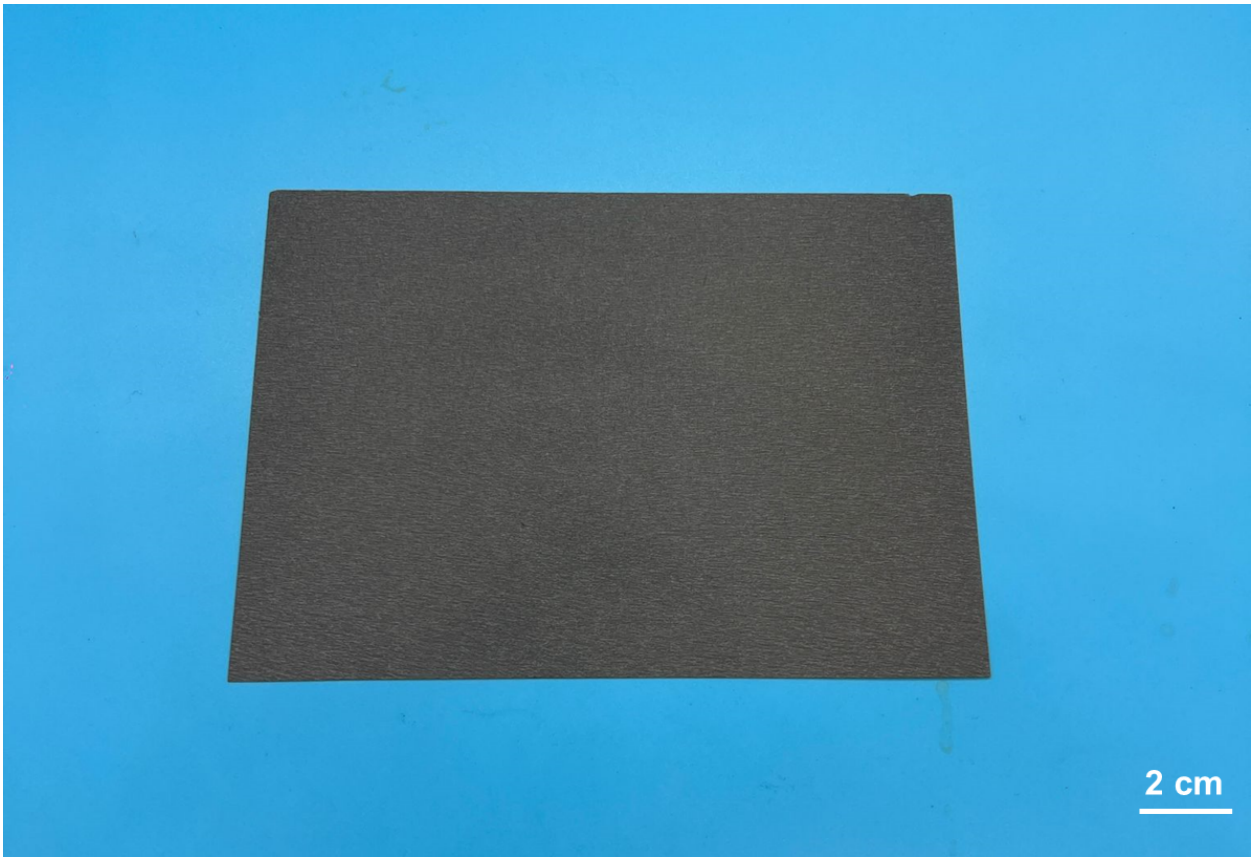

Figure S1. Photo of commercial carbon paper.

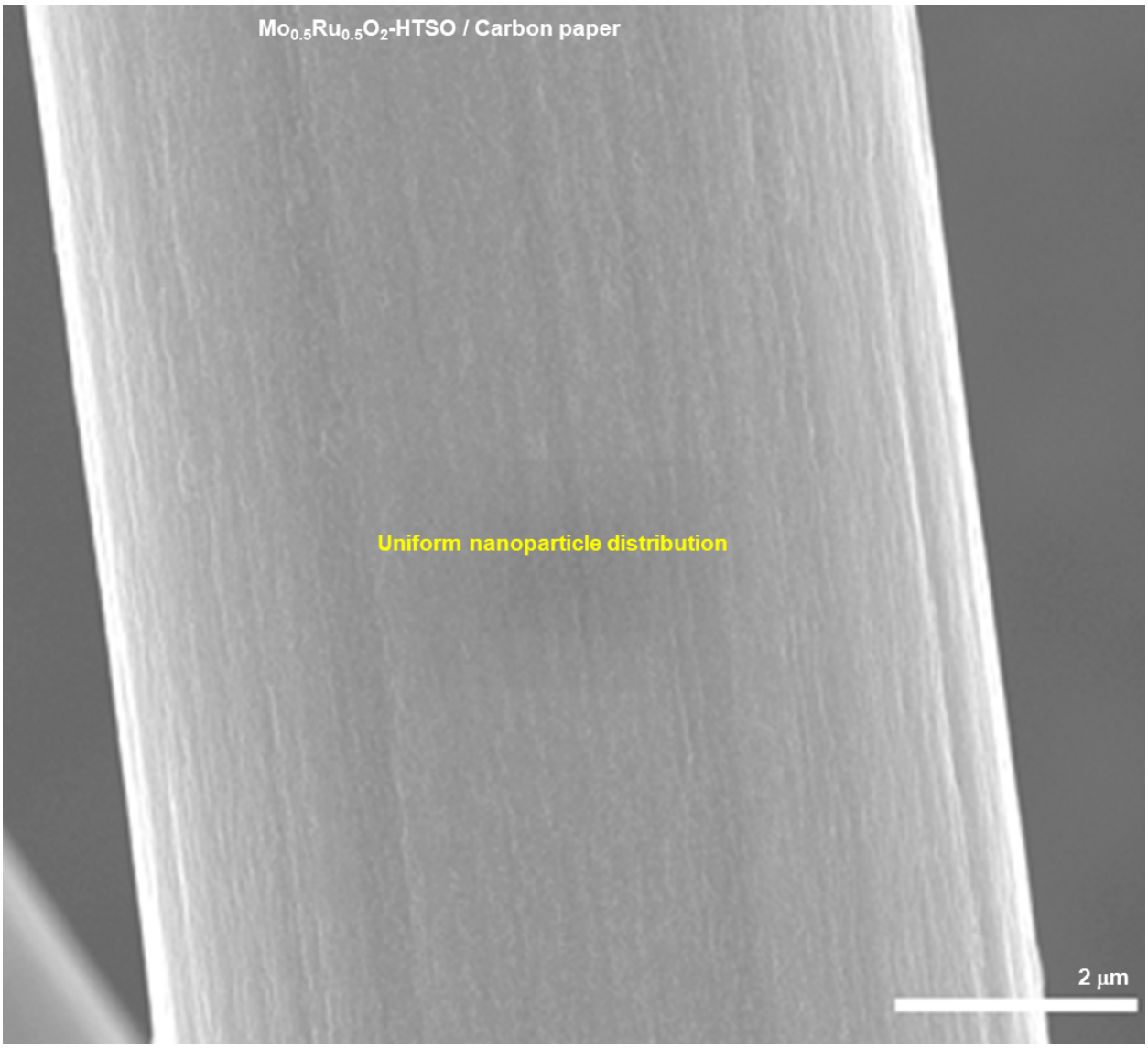

Figure S2. SEM image of $Mo_{0.5}Ru_{0.5}O_2$-HTSO nanoparticles dispersed on carbon paper. The nanoparticles, approximately 10 nm in size, are uniformly distributed across the carbon paper substrate.

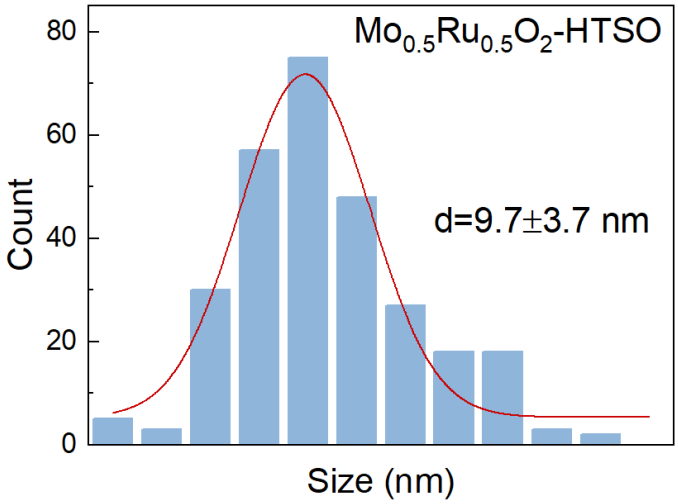

Figure S3. Particle distribution of $Mo_{0.5}Ru_{0.5}O_2$ nanoparticles. The sample of $Mo_{0.5}Ru_{0.5}O_2$-HTSO shows an average particle size of ~10 nm.

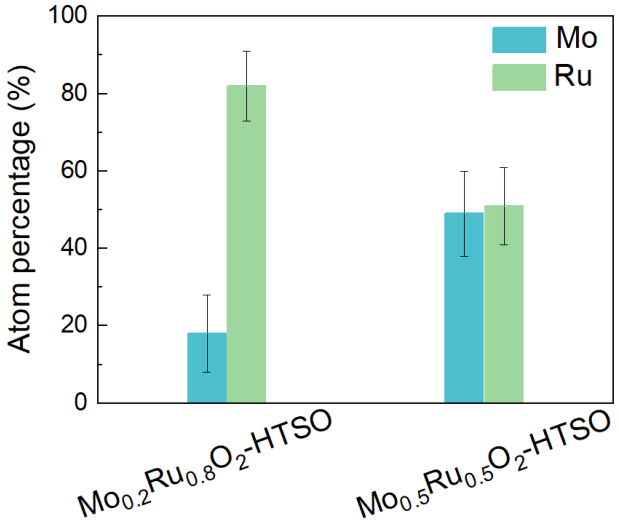

Figure S4. ICP results of fresh $Mo_{0.2}Ru_{0.8}O_2$ and $Mo_{0.5}Ru_{0.5}O_2$. Error bars represent the standard deviation from three independent measurements. The atomic ratios of Ru to Mo in the $Mo_{0.2}Ru_{0.8}O_2$-HTSO and $Mo_{0.5}Ru_{0.5}O_2$-HTSO samples closely matched the intended composition.

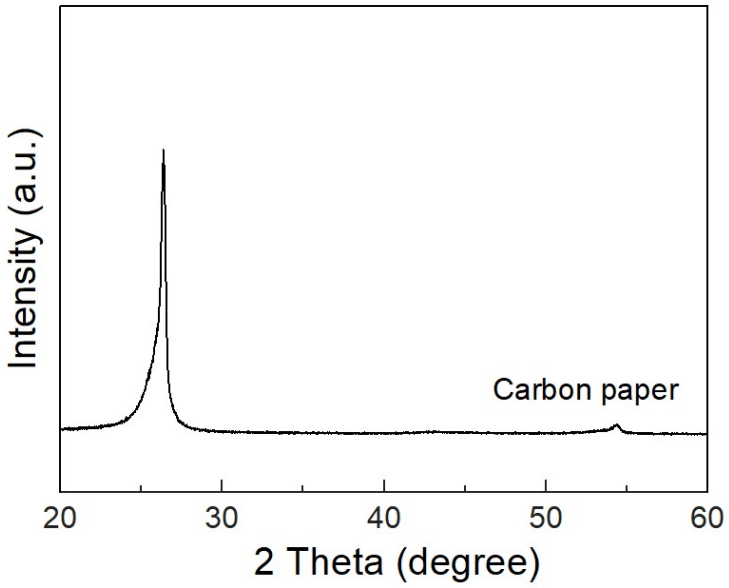

Figure S5. XRD of carbon paper. Signals at 25.9° and 54.5° were attributed to the carbon paper substrate.

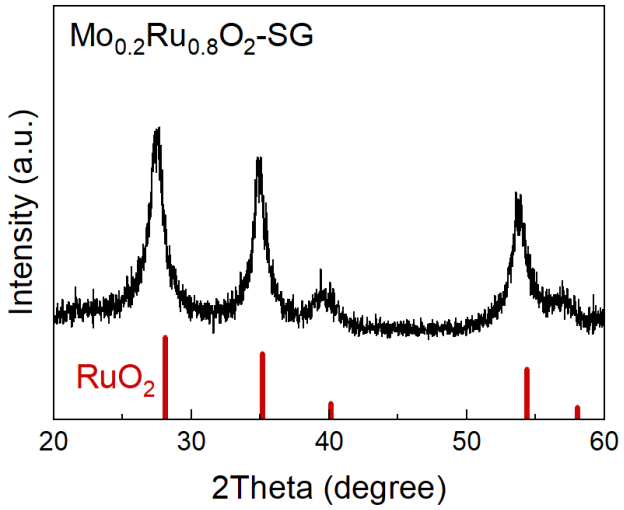

Figure S6. XRD of $Mo_{0.2}Ru_{0.8}O_2$-SG. $Mo_{0.2}Ru_{0.8}O_2$-SG exhibited a single-phase structure, as indicated by diffraction peaks similar to those of RuO_2.

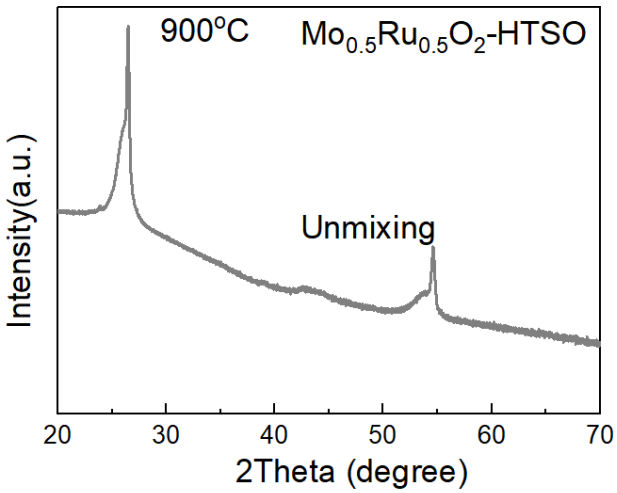

Figure S7. XRD of $Mo_{0.5}Ru_{0.5}O_2$ synthesized at 900 °C. Too low a temperature (*e.g.*, 900 °C) does not promote the mixing of Ru and Mo, while too high a temperature (*e.g.*, 1500 °C) leads to phase separation due to the reduction of Ru at high temperatures *via* carbothermal and high-temperature reduction. Prior studies[1–4] on the RuO_2 formation have shown that higher annealing temperatures improve crystallinity and facilitate solid-solution formation in Ru-based tetragonal oxides, whereas excessively high temperatures can promote the reduction of RuO_2 to metallic Ru, particularly in the presence of carbon or under low oxygen partial pressure, thereby leading to phase segregation.

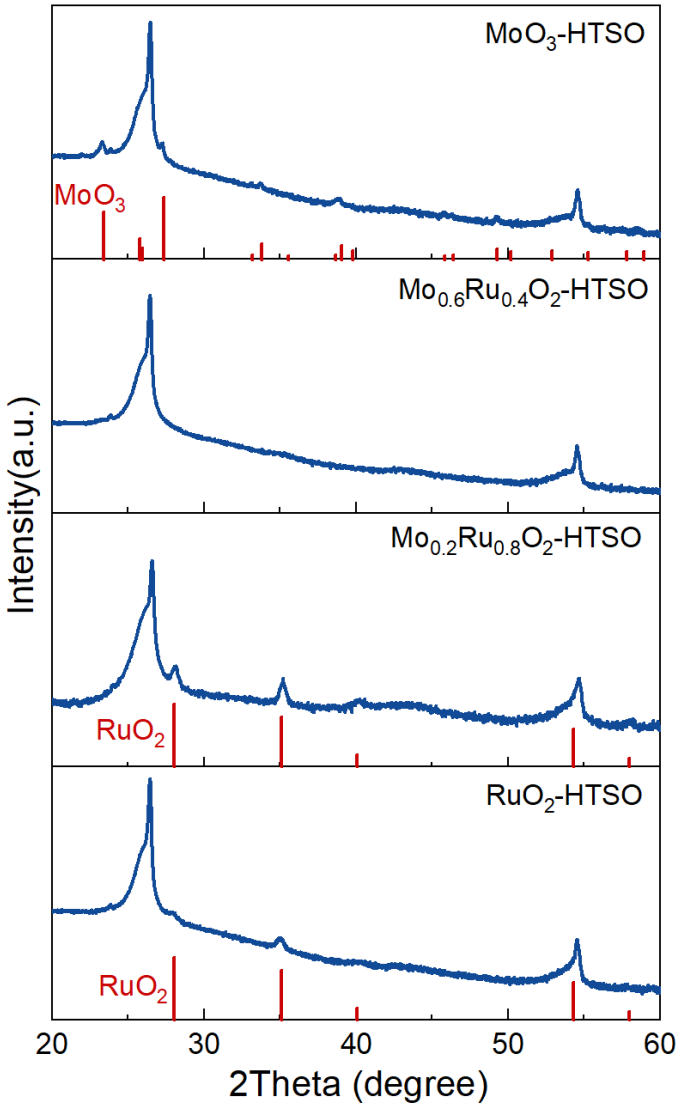

Figure S8. XRD patterns of RuO_2-HTSO, $Mo_{0.2}Ru_{0.8}O_2$-HTSO, $Mo_{0.6}Ru_{0.4}O_2$-HTSO, and MoO_3-HTSO. The XRD patterns of MoO_3-HTSO were consistent with the single-phase orthorhombic structure of MoO_3 (COD: 96-153-7655). The XRD results of RuO_2-HTSO and $Mo_{0.2}Ru_{0.8}O_2$-HTSO matched well with the single-phase tetragonal structure of RuO_2 (COD: 96-100-0059). In contrast, the $Mo_{0.6}Ru_{0.4}O_2$-HTSO sample exhibited no obvious crystalline phase. Excessive Mo content (*e.g.*, $x = 0.6$) disrupted the RuO_2 phase framework, as Mo oxide phases dominated the overall structure, with the maximum doping level for maintaining the RuO_2 framework determined to be $x = 0.5$.

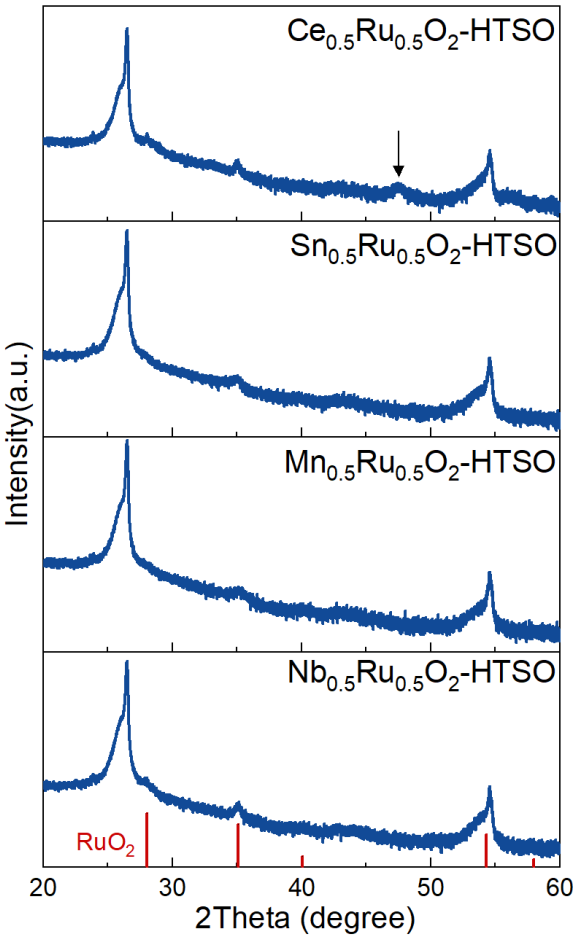

Figure S9. XRD patterns of $Nb_{0.5}Ru_{0.5}O_2$, $Mn_{0.5}Ru_{0.5}O_2$, $Sn_{0.5}Ru_{0.5}O_2$, and $Ce_{0.5}Ru_{0.5}O_2$. $Nb_{0.5}Ru_{0.5}O_2$, $Mn_{0.5}Ru_{0.5}O_2$, and $Sn_{0.5}Ru_{0.5}O_2$ exhibit single-phase structures, with diffraction peaks closely matching those of RuO_2 (Crystallography Open Database, COD: 96-100-0059). In contrast, $Ce_{0.5}Ru_{0.5}O_2$ displays an additional diffraction peak, which can be assigned to CeO_2. This phase segregation arises from the large ionic radius of Ce^{4+} (0.87 Å) relative to Ru^{4+} (0.62 Å), which hinders complete incorporation of Ce into the rutile lattice. By comparison, Mo, Sn, Nb, and Mn have ionic radii much closer to that of Ru^{4+} (Table S1), allowing stable substitution into the RuO_2 lattice and the formation of single-phase solid solutions.

These results demonstrate that, under HTSO process, moderate ionic size mismatches (Mo, Nb, Sn, Mn) can be accommodated to yield homogeneous solid solutions at doping levels up to 50 at%, whereas excessively large mismatches (Ce) result in phase separation at the same doping level, even under rapid quenching conditions.

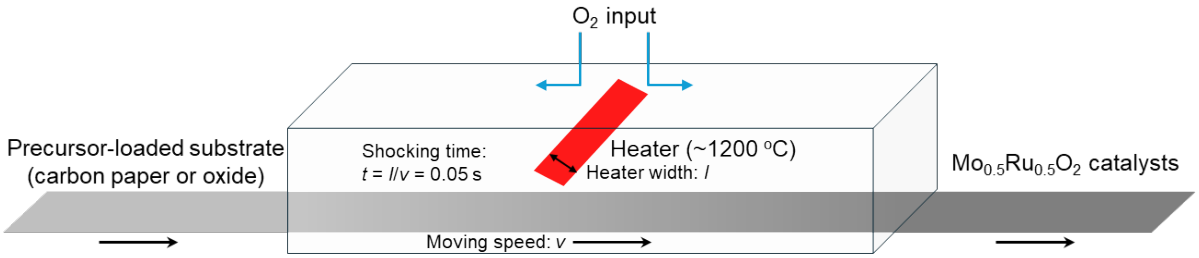

Figure S10. Schematic of our synthesis method for the large-scale production of $Mo_{0.5}Ru_{0.5}O_2$ catalysts. The precursor-loaded substrate is first prepared by mixing Mo and Ru precursor solutions. The dried sample is then placed on a conveyor belt within the furnace. It rapidly passes through a high-temperature heating zone (~1200 °C) under an oxygen atmosphere, simulating the rapid thermal shock process demonstrated the batch-to-batch scale in the laboratory, which leads to the formation of $Mo_{0.5}Ru_{0.5}O_2$ catalysts. Notably, the heating duration (t) in the heating zone is ~0.05 s and can be tuned by adjusting the length (l) of the heating zone and the conveyor belt speed (v), according to the relationship $t = l/v$. Because the synthesis is rapid and the heater is maintained at ~1200 °C without repeated heating and cooling, this approach can further enhance production efficiency and reduce overall cost.

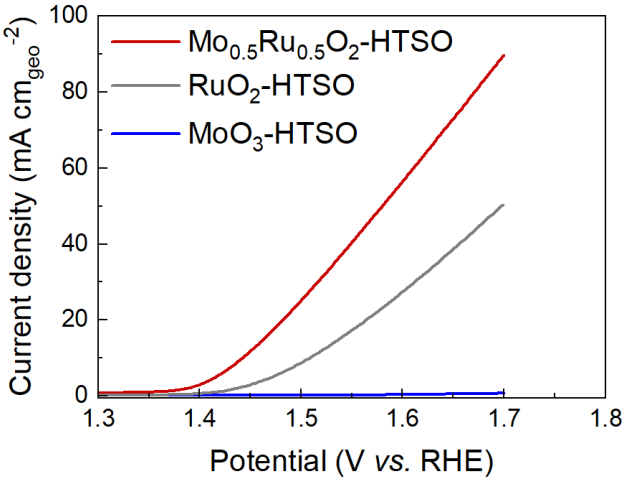

Figure S11. Polarization curves for $Mo_{0.5}Ru_{0.5}O_2$-HTSO, RuO_2-HTSO, and MoO_3-HTSO. MoO_3 itself exhibits almost no activity toward the OER. Therefore, the primary active sites can be attributed to Ru.

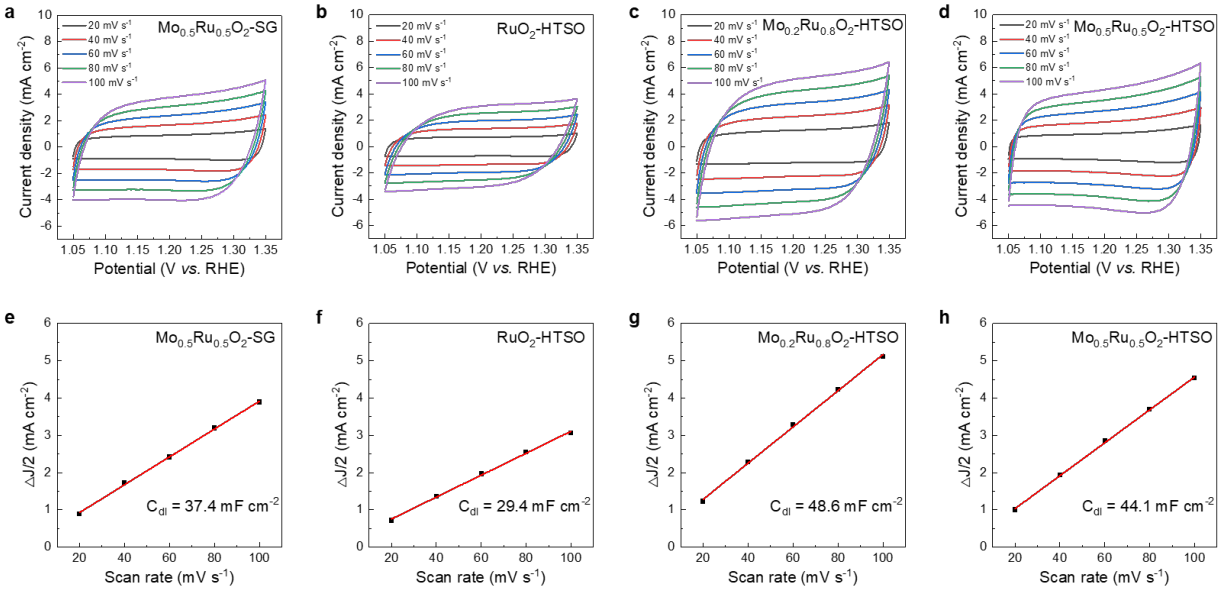

Figure S12. CV curves for (a) $Mo_{0.5}Ru_{0.5}O_2$-SG, (b) RuO_2-HTSO, (c) $Mo_{0.2}Ru_{0.8}O_2$-HTSO, and (d) $Mo_{0.5}Ru_{0.5}O_2$-HTSO from 1.05 to 1.35 V vs. RHE at a scan rate from 20 to 100 mV s^{-1}. C_{dl} plot derived from CV curves for (e) $Mo_{0.5}Ru_{0.5}O_2$-SG, (f) RuO_2-HTSO, (g) $Mo_{0.2}Ru_{0.8}O_2$-HTSO, and (h) $Mo_{0.5}Ru_{0.5}O_2$-HTSO. The electrochemically active surface area (ECSA), derived from the electrochemical double-layer capacitance (C_{dl}) was used to compare the intrinsic activities of $Mo_{0.5}Ru_{0.5}O_2$-SG, RuO_2-HTSO, $Mo_{0.2}Ru_{0.8}O_2$-HTSO, and $Mo_{0.5}Ru_{0.5}O_2$-HTSO.

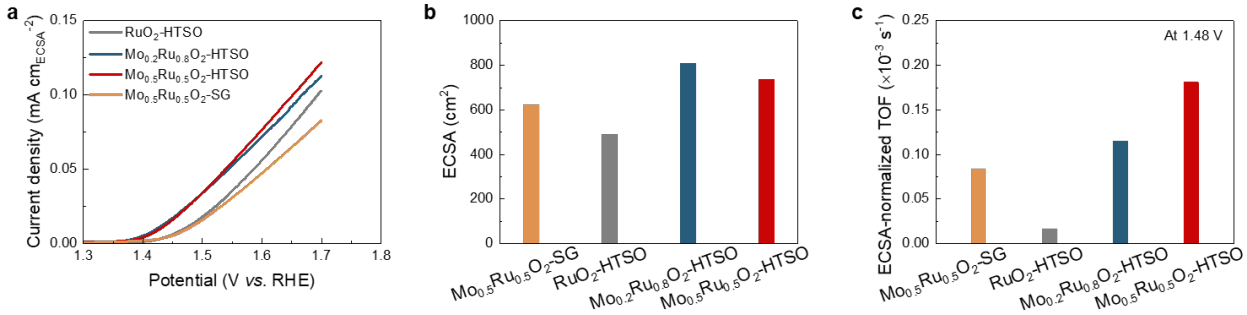

Figure S13. (a) Intrinsic activity normalized on electrochemically active surface area (ECSA), (b) ECSA, and (c) ECSA normalized TOF of $Mo_{0.5}Ru_{0.5}O_2$-SG, RuO_2-HTSO, $Mo_{0.2}Ru_{0.8}O_2$-HTSO, and $Mo_{0.5}Ru_{0.5}O_2$-HTSO. The specific activity (defined as the current density normalized to ECSA) of these catalysts was then calculated, following the order: $Mo_{0.2}Ru_{0.8}O_2$-HTSO > $Mo_{0.5}Ru_{0.5}O_2$-HTSO > $Mo_{0.5}Ru_{0.5}O_2$-SG > RuO_2-HTSO. The ECSA-normalized TOF of $Mo_{0.5}Ru_{0.5}O_2$-HTSO was 0.18×10^{-3} s^{-1}, which is higher than that of $Mo_{0.2}Ru_{0.8}O_2$-HTSO (0.12×10^{-3} s^{-1}) and $Mo_{0.5}Ru_{0.5}O_2$-SG (0.08×10^{-3} s^{-1}).

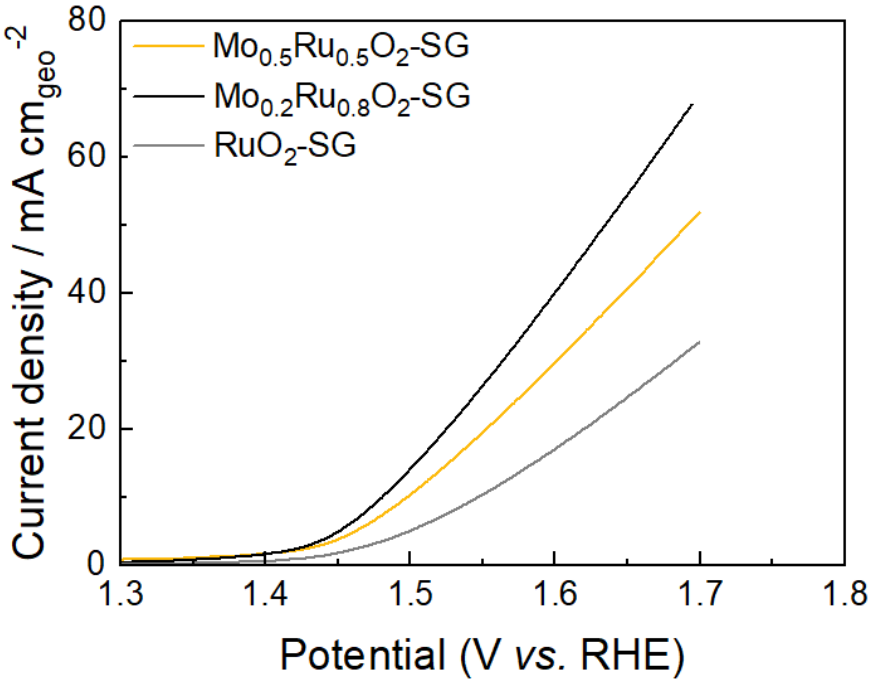

Figure S14. LSV of electrocatalysts synthesized through the sol-gel method. The catalysts include RuO_2-SG, $Mo_{0.2}Ru_{0.8}O_2$-SG, and $Mo_{0.5}Ru_{0.5}O_2$-SG. Mo doping in RuO_2 enhances the catalytic activity compared to pure RuO_2. When comparing $Mo_{0.2}Ru_{0.8}O_2$-SG and $Mo_{0.5}Ru_{0.5}O_2$-SG, the latter demonstrated poorer OER performance.

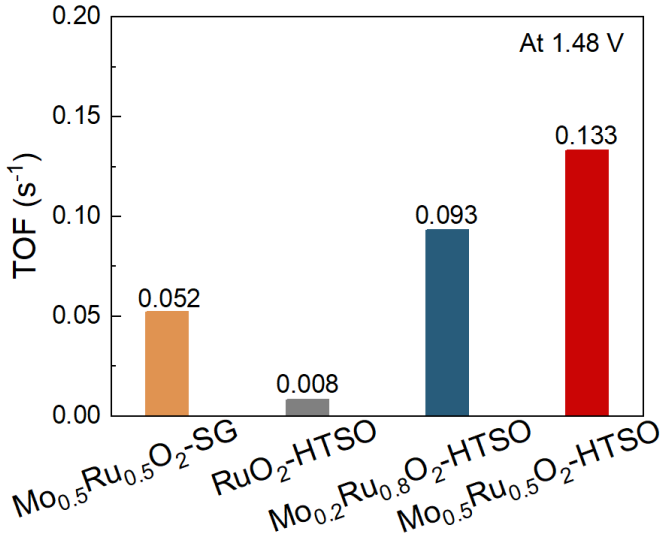

Figure S15. TOF for RuO_2-HTSO, $Mo_{0.2}Ru_{0.8}O_2$-HTSO, $Mo_{0.5}Ru_{0.5}O_2$-HTSO, and $Mo_{0.5}Ru_{0.5}O_2$-SG. The TOF of $Mo_{0.5}Ru_{0.5}O_2$-HTSO was 0.133 s^{-1}, higher than $Mo_{0.2}Ru_{0.8}O_2$-HTSO (0.09 s^{-1}) and much higher than $Mo_{0.5}Ru_{0.5}O_2$-SG (0.033 s^{-1}).

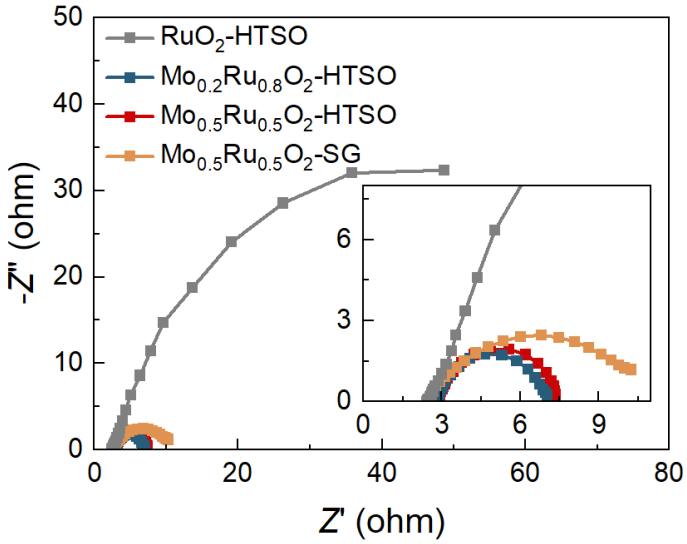

Figure S16. Nyquist plots for RuO_2-HTSO, $Mo_{0.2}Ru_{0.8}O_2$-HTSO, $Mo_{0.5}Ru_{0.5}O_2$-HTSO, and $Mo_{0.5}Ru_{0.5}O_2$-SG, measured over a frequency range of 0.01 Hz to 1.0 MHz at 1.4 V_{RHE}. $Mo_{0.2}Ru_{0.8}O_2$-HTSO and $Mo_{0.5}Ru_{0.5}O_2$-HTSO exhibited similarly low charge transfer resistance, suggesting enhanced OER kinetics compared to $Mo_{0.5}Ru_{0.5}O_2$-SG and RuO_2-HTSO.

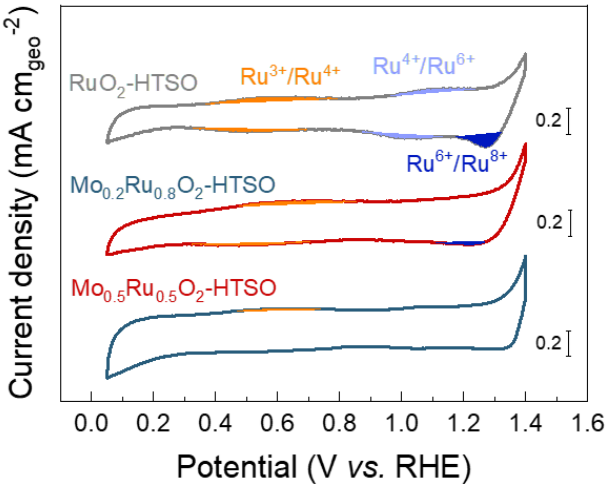

Figure S17. Cycling voltammogram (CV) analysis of the redox peaks for RuO_2-HTSO, $Mo_{0.2}Ru_{0.8}O_2$-HTSO, and $Mo_{0.5}Ru_{0.5}O_2$-HTSO, measured from 0.05 to 1.7 V *vs.* RHE. The oxidation behavior of Ru at elevated overpotentials was investigated by CV in the potential range of 0.05–1.7 V vs. RHE at a scan rate of 10 mV s^{-1} for RuO_2-HTSO, $Mo_{0.2}Ru_{0.8}O_2$-HTSO, and $Mo_{0.5}Ru_{0.5}O_2$-HTSO. For RuO_2-HTSO, two distinct redox couples appeared at ~0.55 and ~1.16 V_{RHE}, which are attributed to the Ru^{3+}/Ru^{4+} and Ru^{4+}/Ru^{6+} transitions, respectively.[5,6] Upon Mo incorporation, the Ru^{3+}/Ru^{4+} transition became more pronounced relative to the Ru^{4+}/Ru^{6+} process, suggesting that the prevailing oxidation state of Ru in Mo-doped samples lies between +3 and +4, consistent with XPS observations. Notably, the redox feature associated with the Ru^{4+}/Ru^{6+} couple diminished significantly at high Mo content, accompanied by the disappearance of the peak near 1.27 V_{RHE}, which is ascribed to the Ru^{6+}/Ru^{8+} transition originating from metastable dissolution intermediates such as $RuO_2(OH)$.[5,6] These results demonstrate that excessive oxidation of Ru centers toward higher valence states during OER is effectively restrained. Consequently, the modified electronic configuration reduces the OER energy barrier and mitigates Ru over-oxidation, thereby enhancing both catalytic activity and durability.

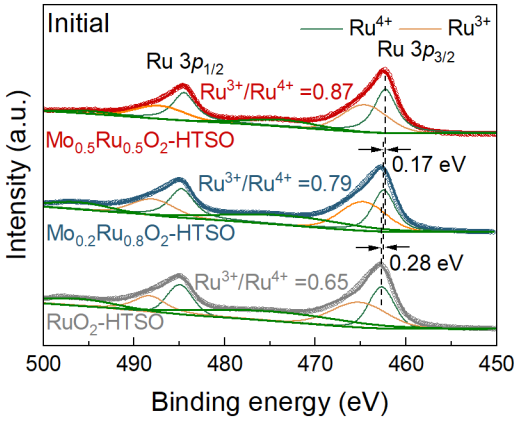

Figure S18. XPS spectra of Ru 3*p* for RuO_2-HTSO, $Mo_{0.2}Ru_{0.8}O_2$-HTSO, and $Mo_{0.5}Ru_{0.5}O_2$-HTSO. The Ru 3*p* spectra were deconvoluted into four peaks. Details can be found in Supplementary Table S1. Notably, the Ru 3*p* peaks in the Mo-doped samples exhibited negative shifts of 0.28 eV ($Mo_{0.2}Ru_{0.8}O_2$-HTSO) and 0.45 eV ($Mo_{0.5}Ru_{0.5}O_2$-HTSO) compared to pure RuO_2-HTSO, indicating a reduction in Ru–O bond covalency due to Mo incorporation. As the Mo doping level increased from 20 at% to 50 at%, the Ru^{3+}/Ru^{4+} ratio increased from 0.79 to 0.87, suggesting that Mo promotes the formation of reduced Ru species. The Ru^{3+}/Ru^{4+} ratio increases with increasing Mo doping content, indicating that a higher amount of doped Mo transfers more electrons to Ru.

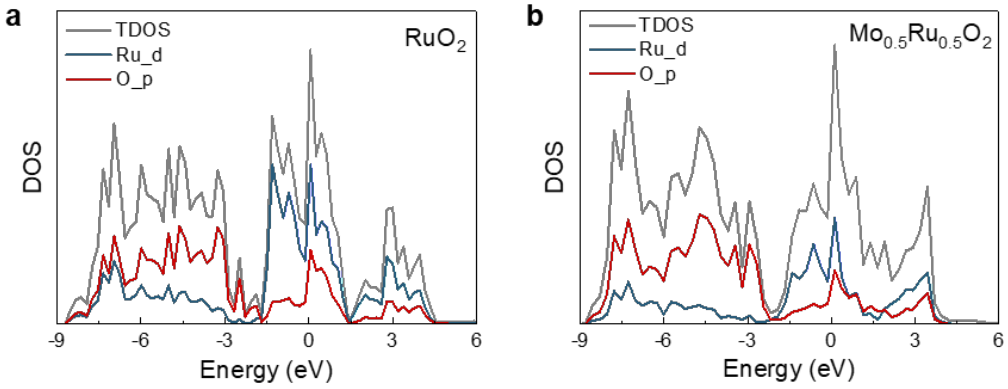

Figure S19. Density of states (DOS) spectra for (a) pristine RuO_2 and (b) $Mo_{0.5}Ru_{0.5}O_2$. The DOS analysis of RuO_2 and $Mo_{0.5}Ru_{0.5}O_2$ reveals clear electronic structure modifications upon Mo doping. Compared to pristine RuO_2, the $Mo_{0.5}Ru_{0.5}O_2$ system exhibits a pronounced reduction in the height difference between Ru *d*-orbital peaks, particularly the diminished contrast between the left and center peaks in the DOS spectrum. In $Mo_{0.5}Ru_{0.5}O_2$, the incorporation of Mo introduces delocalized Ru states at the Fermi level (E_{Fermi}), providing additional conduction pathways that enhance the material's electrical conductivity. Moreover, the *d*-band center values of Ru are -1.61 eV and -1.83 eV in RuO_2 and $Mo_{0.5}Ru_{0.5}O_2$, respectively. The negative shift of the *d*-band center weakens the binding strength between the catalyst surface and the intermediates, thereby facilitating the desorption of the species and improving the overall reaction kinetics of the Mo-doped RuO_2 catalyst.

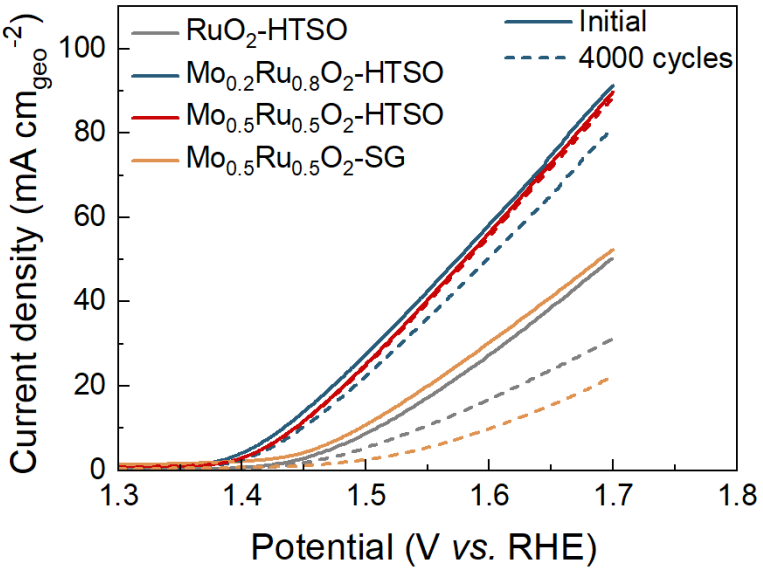

Figure S20. The cyclic voltammetry (CV) tests of RuO_2-HTSO, $Mo_{0.2}Ru_{0.8}O_2$-HTSO, $Mo_{0.5}Ru_{0.5}O_2$-HTSO, $Mo_{0.5}Ru_{0.5}O_2$-SG. OER polarization curves before and after 4000 cycles. The potential windows between 1.3 and 1.7 V_{RHE} in 0.1 M $HClO_4$ solution.

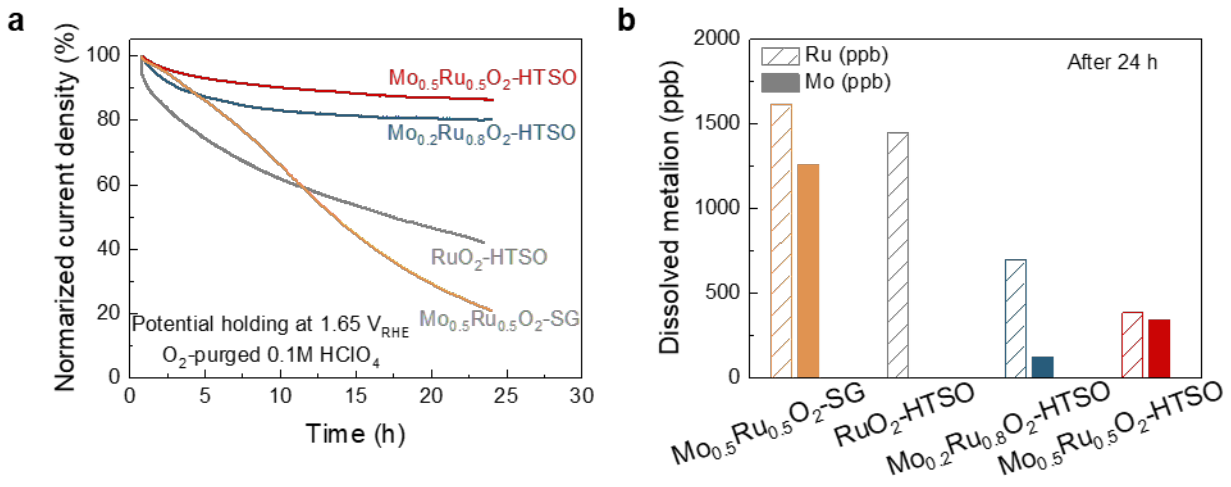

Figure S21. Chronoamperometry (CA) tests of RuO_2-HTSO, $Mo_{0.2}Ru_{0.8}O_2$-HTSO, $Mo_{0.5}Ru_{0.5}O_2$-HTSO, $Mo_{0.5}Ru_{0.5}O_2$-SG. a) Chronoamperometry (CA) tests at 1.65 V_{RHE} indicate that 86.3% of the initial current density remains for $Mo_{0.5}Ru_{0.5}O_2$-HTSO, which is significantly higher than that of $Mo_{0.2}Ru_{0.8}O_2$-HTSO (80.1%), RuO_2-HTSO (42.1%), and $Mo_{0.5}Ru_{0.5}O_2$-SG (20.9%); b) The concentrations of dissolved Ru and Mo ions in the electrolyte after the CA test at 1.65 V_{RHE} for 24 h were analyzed by inductively coupled plasma optical emission spectrometry (ICP-OES). The concentration of dissolved Ru ions of $Mo_{0.5}Ru_{0.5}O_2$-HTSO is much lower than that of $Mo_{0.2}Ru_{0.8}O_2$-HTSO, $Mo_{0.5}Ru_{0.5}O_2$-SG, indicating that the doping of Mo can stabilize Ru and thereby improve the electrocatalytic stability of the catalyst.

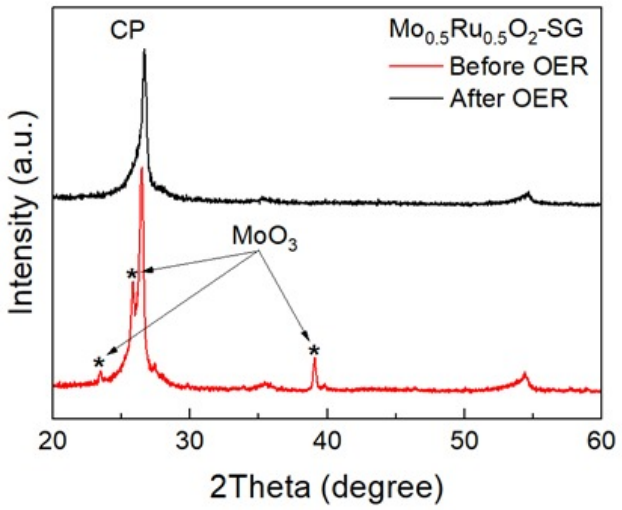

Figure S22. XRD patterns of $Mo_{0.5}Ru_{0.5}O_2$-SG nanoparticles distributed on carbon paper before and after the OER. Diffraction peaks of MoO_3 disappeared after OER, indicating that unstable MoO_3 was dissolved during acidic OER conditions.

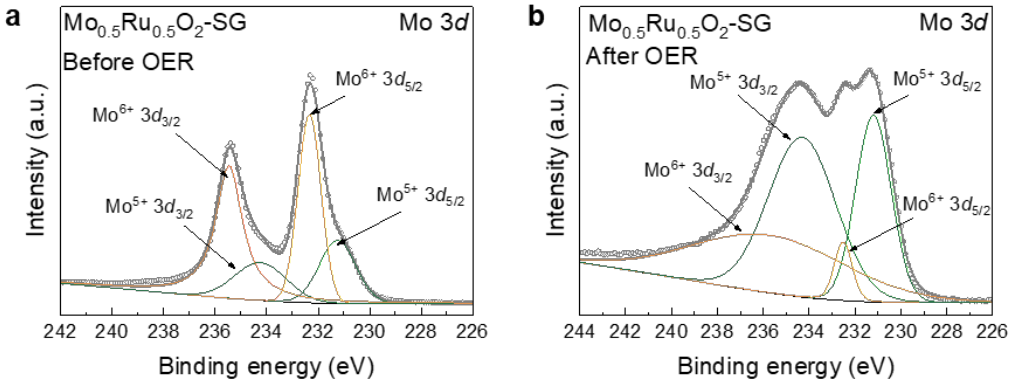

Figure S23. Mo 3*d* XPS spectra of $Mo_{0.5}Ru_{0.5}O_2$-SG (a) before and (b) after the OER test. Detailed XPS results are summarized in Table S3. The Mo 3*d* spectrum can be deconvoluted into four peaks corresponding to Mo^{6+} $3d_{3/2}$, Mo^{5+} $3d_{3/2}$, Mo^{6+} $3d_{5/2}$, and Mo^{5+} $3d_{5/2}$. Compared with the sample before the OER test (Mo^{6+}/Mo^{5+} ratio = 2.28), the ratio after the OER test decreases to 0.54, indicating a reduction of Mo^{6+} species and a significant loss of MoO_3 content.

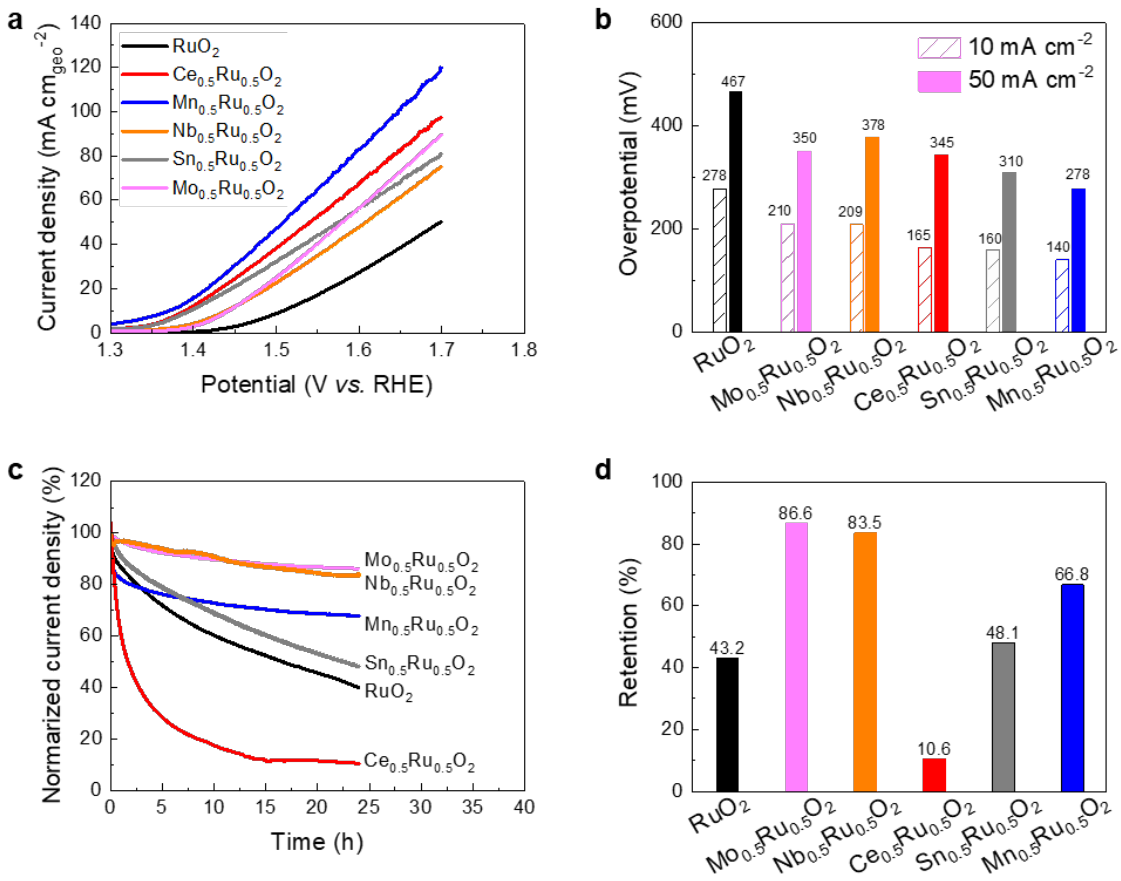

Figure S24. OER activity and stability test for $M_{0.5}Ru_{0.5}O_2$ (M = Ce, Mn, Nb, Sn, Mo). (a) Polarization curves, (b) overpotentials at 10 mA cm^{-2} and 50 mA cm^{-2}, (c) Chronoamperometry (CA) tests at 1.65 V_{RHE} for 24 h, (d) retention (%). The synthesis and evaluation protocols for $Nb_{0.5}Ru_{0.5}O_2$, $Mn_{0.5}Ru_{0.5}O_2$, $Sn_{0.5}Ru_{0.5}O_2$, and $Ce_{0.5}Ru_{0.5}O_2$ were identical to those used for $Mo_{0.5}Ru_{0.5}O_2$. We further evaluated their catalytic activity and stability for the OER. The activity trend followed the order: Mn > Sn > Ce > Nb ≈ Mo > pristine RuO_2. Notably, $Mn_{0.5}Ru_{0.5}O_2$ exhibited an exceptionally low overpotential of 140 mV at 10 mA cm^{-2}, which is likely attributable to the intrinsically high OER activity of Mn species.[7] Durability was subsequently assessed under a constant potential of 1.65 V_{RHE} for 24 h. $Nb_{0.5}Ru_{0.5}O_2$ showed excellent durability, retaining 83.5% of its activity, second only to Mo, consistent with recent reports.[8] In contrast, despite their high initial activity, Mn-, Sn-, and Ce-doped samples exhibited severe instability, with the Ce-doped catalyst undergoing drastic performance decay. The instability of Sn- and Mn-doped samples is likely associated with their multiple low oxidation states (e.g., 2^+–4^+), which can generate unstable surface oxides prone to dissolution or leaching, and which do not provide sufficient electron transfer to Ru to suppress Ru over-oxidation. For Ce, the instability can be rationalized by its large ionic radius (Ce^{4+}: 0.97 Å) compared to Ru^{4+} (0.62 Å). This substantial size mismatch may induce lattice distortion and the formation of a separate CeO_2 phase, thereby accelerating degradation. Taken together, these results highlight the unique structural features of $Mo_{0.5}Ru_{0.5}O_2$-HTSO that enable both high OER activity and outstanding durability.

Table S1. Ionic radii comparison (CN = 6) of different elements.

Element	Oxidation state	Ionic radius (Å)	Relative to Ru^{4+} (0.62 Å)
Ru	+4	0.62	/
	+3	0.68	Slightly larger
Mo	+6	0.59	Slightly smaller
	+5	0.61	Very close
Nb	+5	0.64	Very close
Mn	+4	0.53	Smaller
	+3	0.65	Close
Sn	+4	0.69	Larger
Ce	+4	0.87	Much larger

Table S2. Fitting results of the Ru 3*p* XPS spectra of RuO_2-HTSO, $Mo_{0.2}Ru_{0.8}O_2$-HTSO, and $Mo_{0.5}Ru_{0.5}O_2$-HTSO before and after the OER stability tests.

Samples	Ru^{4+} ($3p_{3/2}$)		Ru^{3+} ($3p_{3/2}$)		Ru^{4+} ($3p_{1/2}$)		Ru^{3+} ($3p_{1/2}$)		Ratio of Ru^{3+}/Ru^{4+}
	Position /eV	Area	Position /eV	Area	Position /eV	Area	Position /eV	Area	
RuO_2-HTSO (Before OER)	462.7	374.6	465.8	181.5	484.6	142.1	487.0	157.1	0.65
RuO_2-HTSO (After OER)	462.7	341.3	465.2	262.3	485.0	262.3	488.3	73.0	0.42
$Mo_{0.2}Ru_{0.8}O_2$-HTSO (Before OER)	462.4	281.6	464.6	265.5	484.6	210.4	487.8	124.3	0.79
$Mo_{0.2}Ru_{0.8}O_2$-HTSO (After OER)	462.5	329.5	465.0	270.4	484.8	232.8	488.0	113.2	0.68
$Mo_{0.5}Ru_{0.5}O_2$-HTSO (Before OER)	462.3	292.2	464.6	272.1	484.5	186.0	487.2	145.4	0.87
$Mo_{0.5}Ru_{0.5}O_2$-HTSO (After OER)	462.1	268.4	464.4	249.7	484.3	240.4	487.2	172.5	0.83

Table S3. Fitting results of the Mo 3*d* XPS spectra of $Mo_{0.5}Ru_{0.5}O_2$-SG and $Mo_{0.5}Ru_{0.5}O_2$-HTSO before and after the OER test.

Samples	Mo^{5+} $3d_{5/2}$		Mo^{6+} $3d_{5/2}$		Mo^{5+} $3d_{3/2}$		Mo^{6+} $3d_{3/2}$		Ratio of Mo^{6+}/Mo^{5+}
	Position/eV	Area	Position/eV	Area	Position/eV	Area	Position/eV	Area	
$Mo_{0.5}Ru_{0.5}O_2$-SG, Before	231.3	49.4	232.3	92.8	234.2	41.6	235.5	114.4	2.28
$Mo_{0.5}Ru_{0.5}O_2$-SG, After	231.2	160.7	232.5	26.9	234.3	261.0	235.8	201.7	0.54
$Mo_{0.5}Ru_{0.5}O_2$-HTSO, Before	230.8	127.6	232.2	129.3	234.2	188.3	235.4	144.0	0.87
$Mo_{0.5}Ru_{0.5}O_2$-HTSO, After	230.9	103.9	232.4	152.1	234.4	158.7	235.6	165.8	1.21

The Mo *3d* spectrum can be deconvoluted into four peaks. In the $Mo_{0.5}Ru_{0.5}O_2$-HTSO sample before the OER test, the peaks at 230.8 and 234.2 eV correspond to Mo^{5+} $3d_{5/2}$ and Mo^{5+} $3d_{3/2}$, respectively, while the peaks at 232.3 and 235.4 eV are assigned to Mo^{6+} $3d_{5/2}$ and Mo^{6+} $3d_{3/2}$, respectively. These results demonstrate the coexistence of multivalent Mo species (Mo^{5+} and Mo^{6+}) in $Mo_{0.5}Ru_{0.5}O_2$-HTSO.

Table S4. Performance comparison between our developed $Mo_{0.5}Ru_{0.5}O_2$ catalyst and state-of-the-art RuO_2-based OER catalysts.

Catalysts	Dopant	Overpotential (mV)	Current density (mA cm^{-2})	Time (h)	Potential drop (mV)	Decay (mV/h)	Electrolyte
$Mg_{0.05}Ru_{0.95}O_2$[9]	Mg	228	10	30	140	4.67	0.5M H_2SO_4
$Si_{0.1}Ru_{0.9}O_2$[10]	Si	226	10	800	42	0.053	0.1M $HClO_4$
$Cr_{0.6}Ru_{0.4}O_2$[11]	Cr	178	10	10	70.8	7.1	0.5M H_2SO_4
$Mn_{0.06}Ru_{0.94}O_2$[12]	Mn	158	10	10	194	19.4	0.5M H_2SO_4
$Co_{0.11}Ru_{0.89}O_2$[13]	Co	169	10	50	62	1.24	0.5M H_2SO_4
$Ni_{0.25}Ru_{0.75}O_2$[14]	Ni	214	10	220	19.3	0.088	0.1M $HClO_4$
$Cu_{0.13}Ru_{0.87}O_2$[15]	Cu	188	10	8	83	10.375	0.5M H_2SO_4
$Zn_{0.05}Ru_{0.95}O_2$[16]	Zn	173	50	100	90	0.9	0.5M H_2SO_4
$Nb_{0.1}Ru_{0.9}O_2$[8]	Nb	204	200	360	9	0.025	0.5M H_2SO_4
$Mo_{0.15}Ru_{0.85}O_2$[17]	Mo	147	10	20	136	6.8	0.5M H_2SO_4
$Rh_{0.02}Ru_{0.98}O_2$[18]	Rh	161	50	700	34.1	0.049	0.5M H_2SO_4
$Sn_{0.5}Ru_{0.5}O_2$[19]	Sn	194	100	250	26.8	0.107	0.5M H_2SO_4
$Nd_{0.1}Ru_{0.9}O_2$[20]	Nd	211	10	25	26.4	1.056	0.5M H_2SO_4
$Er_{0.09}Ru_{0.91}O_2$[21]	Er	200	10	200	53.7	0.269	0.5M H_2SO_4
$Re_{0.06}Ru_{0.94}O_2$[22]	Re	190	10	200	65	0.325	0.1M $HClO_4$
$W_{0.2}Er_{0.1}Ru_{0.7}O_2$[23]	W-Er	168	10	500	90	0.18	0.5M H_2SO_4
$Mo_{0.2}Ce_{0.2}Ru_{0.6}O_2$[24]	Mo-Ce	164	100	100	81	0.81	0.5M H_2SO_4
$Pd_{0.01}Co_{0.02}Ru_{0.97}O_2$[25]	Pd-Co	190	100	200	14.4	0.072	0.5M H_2SO_4
$Nb_{0.1}Mn_{0.1}Ru_{0.8}O_2$[26]	Nb-Mn	209	200	400	32	0.08	0.5M H_2SO_4
$Mo_{0.5}Ru_{0.5}O_2$ This work	**Mo**	**208**	**50**	**300**	**18**	**0.06**	**0.1M $HClO_4$**

Supplementary References

[1] T. B. Reed, *Free Energy of Formation of Binary Compounds*, MIT Press, **1971**.

[2] N. J. Stedman, A. K. Cheethamb, P. D. Battle, *J. Mater. Chem.* **1994**, *4*, 641.

[3] M. Angermann, G. Jakopic, C. Prietl, T. Griesser, K. Reichmann, M. Deluca, *Journal of Sol-Gel Science and Technology* **2023**, *108*, 575.

[4] F. Kwofie, Z. He, W. Zeng, M. Gao, Y. Li, J. Zhang, Y. Li, Y. Liu, Q. Meyer, C. Zhao, Y. Cheng, *Electrochimica Acta* **2025**, *512*, 145442.

[5] R. Kötz, S. Stucki, D. Scherson, D. M. Kolb, *Journal of Electroanalytical Chemistry* **1984**, *172*, 211.

[6] N. Cong, Y. Han, L. Tan, C. Zhai, H. Chen, J. Han, H. Fang, X. Zhou, Y. Zhu, Z. Ren, *Journal of Electroanalytical Chemistry* **2021**, *881*, 114955.

[7] L. Tan, X. Wu, H. Wang, J. Zeng, B. Mei, X. Pan, W. Hu, M. Faiza, Q. Xiao, Y. Zhao, C. Fu, C. Lin, X. Li, W. Luo, *ACS Catalysis* **2024**, *14*, 11273.

[8] H. Liu, Z. Zhang, J. Fang, M. Li, M. G. Sendeku, X. Wang, H. Wu, Y. Li, J. Ge, Z. Zhuang, D. Zhou, Y. Kuang, X. Sun, *Joule* **2023**, *7*, 558.

[9] Z. Li, S. Wang, Y. Tian, B. Li, H. J. Yan, S. Zhang, Z. Liu, Q. Zhang, Y. Lin, L. Chen, *Chemical Communications* **2020**, *56*, 1749.

[10] X. Ping, Y. Liu, L. Zheng, Y. Song, L. Guo, S. Chen, Z. Wei, *Nature Communications* **2024**, *15*, 2501.

[11] Y. Lin, Z. Tian, L. Zhang, J. Ma, Z. Jiang, B. J. Deibert, R. Ge, L. Chen, *Nature Communications* **2019**, *10*, 162.

[12] S. Chen, H. Huang, P. Jiang, K. Yang, J. Diao, S. Gong, S. Liu, M. Huang, H. Wang, Q. Chen, *ACS Catalysis* **2020**, *10*, 1152.

[13] Y. Tian, S. Wang, E. Velasco, Y. Yang, L. Cao, L. Zhang, X. Li, Y. Lin, Q. Zhang, L. Chen, *iScience* **2020**, *23*, 100756.

[14] Z. Y. Wu, F. Y. Chen, B. Li, S. W. Yu, Y. Z. Finfrock, D. M. Meira, Q. Q. Yan, P. Zhu, M. X. Chen, T. W. Song, Z. Yin, H. W. Liang, S. Zhang, G. Wang, H. Wang, *Nature Materials* **2023**, *22*, 100.

[15] J. Su, R. Ge, K. Jiang, Y. Dong, F. Hao, Z. Tian, G. Chen, L. Chen, *Advanced Materials* **2018**, *30*, 1801351.

[16] D. Zhang, M. Li, X. Yong, H. Song, G. I. N. Waterhouse, Y. Yi, B. Xue, D. Zhang, B. Liu, S. Lu, *Nature Communications* **2023**, *14*, 2517.

[17] Y. Zhang, J. Dong, T. Sun, X. Zhang, J. Chen, L. Xu, *Small* **2024**, *20*, 1.

[18] Y. Wang, R. Yang, Y. Ding, B. Zhang, H. Li, B. Bai, M. Li, Y. Cui, J. Xiao, Z. S. Wu, *Nature Communications* **2023**, *14*, 1412.

[19] Z. Shi, J. Li, Y. Wang, S. Liu, J. Zhu, J. Yang, X. Wang, J. Ni, Z. Jiang, L. Zhang, Y. Wang, C. Liu, W. Xing, J. Ge, *Nature Communications* **2023**, *14*, 843.

[20] L. Li, G. Zhang, J. Xu, H. He, B. Wang, Z. Yang, S. Yang, *Advanced Functional Materials* **2023**, *33*, 2213304.

[21] L. Li, G. Zhang, C. Zhou, F. Lv, Y. Tan, Y. Han, H. Luo, D. Wang, Y. Liu, C. Shang, L. Zeng, Q. Huang, R. Zeng, N. Ye, M. Luo, S. Guo, *Nature Communications* **2024**, *15*, 4974.

[22] H. Jin, X. Liu, P. An, C. Tang, H. Yu, Q. Zhang, H. J. Peng, L. Gu, Y. Zheng, T. Song, K. Davey, U. Paik, J. Dong, S. Z. Qiao, *Nature Communications* **2023**, *14*, 354.

[23] S. Hao, M. Liu, J. Pan, X. Liu, X. Tan, N. Xu, Y. He, L. Lei, X. Zhang, *Nature Communications* **2020**, *11*, 5368.

[24] J. He, W. Li, P. Xu, J. Sun, *Applied Catalysis B: Environmental* **2021**, *298*, 120528.

[25] J. Tang, Q. Zeng, Q. Jiang, H. Wang, S. Hu, Y. Ji, H. Zeng, C. Liu, H. J. Peng, X. Li, T. Zheng, C. W. Pao, X. Liu, C. Xia, *Chem Catalysis* **2025**, *5*, 101441.
[26] B. Yuan, Q. Dang, H. Liu, M. G. Sendeku, J. Peng, Y. Fan, L. Cai, A. Cao, S. Chen, H. Li, Y. Kuang, F. Wang, X. Sun, *Nature Communications* **2025**, *16*, 4583.